Earth and Planetary Science Letters 339-340 (2012) 57–66

Contents lists available at SciVerse ScienceDirect

Earth and Planetary Science Letters

journal homepage: www.elsevier.com/locate/epsl

Quartz shielding of sub-10 μm zircons from radiation damage-enhanced Pb loss: An example from a metamorphosed mafic dike, northwestern Wyoming craton

Alexis K. Ault *, Rebecca M. Flowers, Kevin H. Mahan

Department of Geological Sciences, University of Colorado at Boulder, 2200 Colorado Avenue, UCB 399 Boulder, CO 80309, USA

ARTICLE INFO

Article history:
Received 21 October 2011
Received in revised form
6 April 2012
Accepted 17 April 2012
Editor: B. Marty
Available online 2 July 2012

Keywords:
in situ SIMS U–Pb geochronology
zircon
shielding
Pb loss
radiation damage
mafic dike

ABSTRACT

The coupling of two new approaches enabled acquisition of in situ U–Pb data from zircons as small as 5 μm in a metamorphosed mafic dike from the Northern Madison Range, Montana. Despite negligible zircon yield by mineral separation, automated mineralogy rapidly identified >375 sub-20 μm zircons in a single thin section. Subsequently, zircon crystals were dated using modifications to the conventional SIMS technique to preferentially collect secondary ions emitted from a domain a few microns in size within the ~20 μm diameter analysis pit. This approach allowed analysis of zircons too small to be dated by standard SIMS and TIMS methods. U–Pb data define a discordia array with upper and lower intercepts of 1753 ± 9 Ma and 63 ± 8 Ma, respectively (1σ error, MSWD = 1.5). We interpret the upper intercept to reflect zircon growth during high-temperature and high-pressure metamorphism (800 °C, 1.2 GPa) based on textural relationships between the dated zircons and the peak metamorphic assemblage. The lower intercept is attributable to the thermal pulse associated with emplacement of the nearby ca. 75 Ma Tobacco Root batholith. Percent discordance is linked with both textural setting and U concentration. Zircons located along grain boundaries or within fractured host grains display a positive correlation between U (1049–2817 ppm) and percent discordance (12–82%) that is consistent with radiation damage-enhanced Pb loss. In contrast, three zircons housed completely within unfractured quartz yield the most concordant analyses of the dataset (≤7% discordant), despite U concentrations comparable to highly discordant matrix grains. This relationship suggests that the included zircons were shielded from Pb loss by the encapsulating quartz crystals. The results imply that targeting zircons located completely within unfractured host phases may aid in isolating earlier portions of geologic histories. The primary geological implication of this dataset is to increase the documented extent of Paleoproterozoic high-grade metamorphism in the northwestern Wyoming craton.

1. Introduction

Zircon U–Pb geochronology is a cornerstone of tectonic studies. Zircons are ideal targets for chronological information because they are common in many rock types, contain relatively high U and Th concentrations but incorporate little Pb upon crystallization, are durable, and are characterized by low U, Th, and Pb diffusivities through the undamaged crystal lattice. Increasingly precise analytical techniques, as well as improvements in spatial resolution, continue to expand the reach of this tool. For example, the analytical precision of 0.1% attained by thermal ionization mass spectrometry methods has dramatically enhanced our ability to calibrate the stratigraphic record (e.g., Bowring and Schmitz, 2003; Ramezani et al., 2011), the rapid throughput of U–Pb dating by laser ablation ICPMS techniques has facilitated detrital zircon geochronology studies to decipher sediment provenance and erosional histories (e.g., Gehrels et al., 2008), and the high spatial resolution of secondary ion mass spectrometry (SIMS) allows precise targeting of specific domains within individual zircon crystals (e.g., Ireland and Williams, 2003). Although most SIMS U–Pb studies are carried out on separated zircons in grain mounts, this method is also especially well-suited for in situ U–Pb dating. Most in situ analytical work has been accomplished on monazite (e.g., Stern and Berman, 2000), with fewer studies on zircon (e.g., Tomkins et al., 2005).

The ability to date increasingly small zircon crystals using SIMS with retention of the petrographic context has a variety of benefits that are specifically exploited in this study. First, this capability enables extraction of age information from samples otherwise difficult to date by the U–Pb method. For example, mafic dike swarms provide critical time markers for tectonometamorphic activity and are useful for unraveling complex geologic histories, but dike samples commonly yield little or no zircon of sufficient size (≥10 μm) for U–Pb analysis. Second, in situ investigation permits the petrologic significance of the zircon

* Corresponding author. Tel.: +1 303 492 6174; fax: +1 303 492 2606.
E-mail address: alexis.ault@colorado.edu (A.K. Ault).

0012-821X/$ - see front matter © 2012 Elsevier B.V. All rights reserved.
http://dx.doi.org/10.1016/j.epsl.2012.04.025

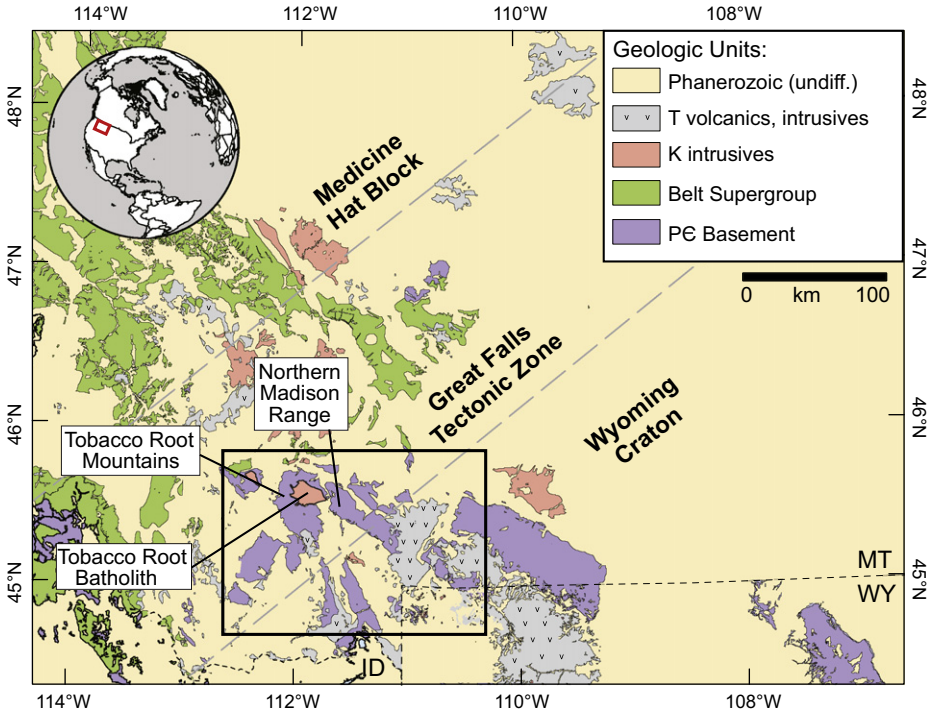

Fig. 1. Simplified regional geologic map of the northern Rocky Mountains of Montana, Idaho, and Wyoming, with basement rocks exposed in Laramide uplifts. Major Precambrian geologic provinces are noted and separated by dashed gray lines. Black box denotes location of Fig. 2A.

dates to be directly linked with the zircon growth history and the pressure–temperature–time evolution of the rock. Finally, these analytical advances may provide insight into aspects of the U–Pb system that have not yet been fully explored. For example, although thermal shielding of zircons included in other phases might be expected to influence the age distribution of U–Pb data from complex polymetamorphic rocks, this effect has not previously been documented. The absence of such datasets may reflect the paucity of U–Pb studies that retain the petrographic context of the analyzed grains.

In this study, we applied two new approaches that together enabled us to acquire geochronological information on zircons from a metamorphosed mafic dike in the Wyoming craton in the Northern Madison Range of southwestern Montana (Figs. 1 and 2). Initial processing of ~40 kg of this sample using conventional crushing, magnetic separation, and heavy liquid methods yielded only two low-quality zircons. In contrast, subsequent application of automated mineralogical analysis of a single thin section from the mafic dike identified over 375 sub-20 μm zircon grains in less than 30 min. U–Pb SIMS geochronology typically uses a spot size of 10–20 μm, exceeding the dimensions of most of our zircon crystals and thus rendering many of our grains undatable by conventional methods. However, advances in SIMS techniques recently allowed dating of in situ baddeleyite grains as small as 3 μm (Chamberlain et al., 2010; Schmitt et al., 2010). Similar application to zircon in our study permitted us to date grains with a minimum dimension of 4 μm. We used this coupled approach to first guide our selection of zircon crystals and then to acquire in situ U–Pb data from a suite of 25 zircons from the thin section. We then utilized these results to (1) characterize the relationship between zircon textural setting, U concentration, and discordance in our dataset, (2) assess the significance of an intriguing association between the most concordant analyses and the occurrence of zircons encapsulated within quartz, and (3) place our chronological data in the context of regional tectonometamorphism along the northwestern margin of the Wyoming craton.

2. Geological setting

The Wyoming craton is characterized by assemblages of geophysically and geochemically distinct Middle and Late Archean rocks (Wooden and Mueller, 1988; Mogk et al., 1992; Frost et al., 1998; Henstock et al., 1998; Chamberlain et al., 2003), exposed in Late Cretaceous–Early Tertiary Laramide-style uplifts. Mafic dike swarms of differing age commonly occur in the basement-cored uplifts and have experienced varying degrees of tectonometamorphism (e.g., Snyder et al., 1988). Age constraints on the emplacement of these swarms include ca. 2.7 Ga in the Beartooth Mountains of Montana associated with Stillwater Complex magmatism (Premo et al., 1990), 2.69 Ga in the Bighorn Mountains of north-central Wyoming (Chamberlain et al., 2010), 2.17 Ga in the Wind River Range of Wyoming (Harlan et al., 2003), 2.09 Ga in the Sierra Madre Mountains of southern Wyoming (Premo and Van Schmus, 1989), 2.06 Ga in the Tobacco Root Mountains of Montana (Mueller et al., 2004), 2.01 Ga in the Laramie Range of Wyoming (Cox et al., 2000), and 1450 Ma and 780 Ma in the Tobacco Root, Ruby, and Highland Mountains of Montana (Harlan et al., 2005).

The Northern Madison Range of southwestern Montana is located along the northwestern margin of the Wyoming craton (Fig. 1). Crystalline basement rocks in the range include 3.5–3.3 Ga orthogneisses (dominantly tonalite–granodiorite–granite) and intercalated paragneisses (e.g., Mueller et al., 1993, 2004), intruded by variably deformed and metamorphosed mafic dikes of unknown age. Recent geochronological studies indicate that regional thermotectonism at 1.78–1.72 Ga, culminating in upper amphibolite to granulite facies metamorphism, affected rocks in the Tobacco Root Mountains and other ranges at the extreme northwestern margin of the Wyoming craton (Fig. 2A; Erslev and Sutter, 1990; Jacob, 1994; King, 1994; Harlan et al., 1996; Kovaric et al., 1996; Brady et al., 1998, 2004; Roberts et al., 2002; Cheney et al., 2004a). However, while Proterozoic thermal resetting of K/Ar and Rb/Sr systems has long been recognized in southwestern

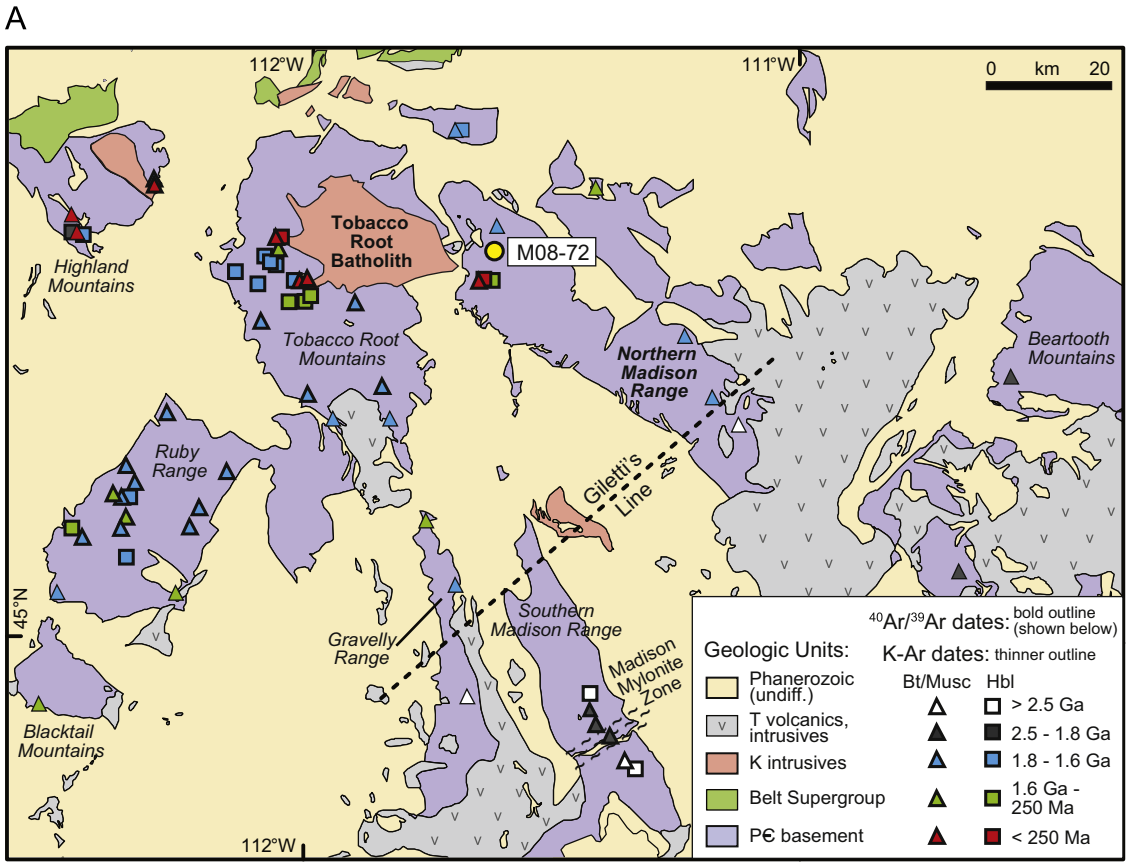

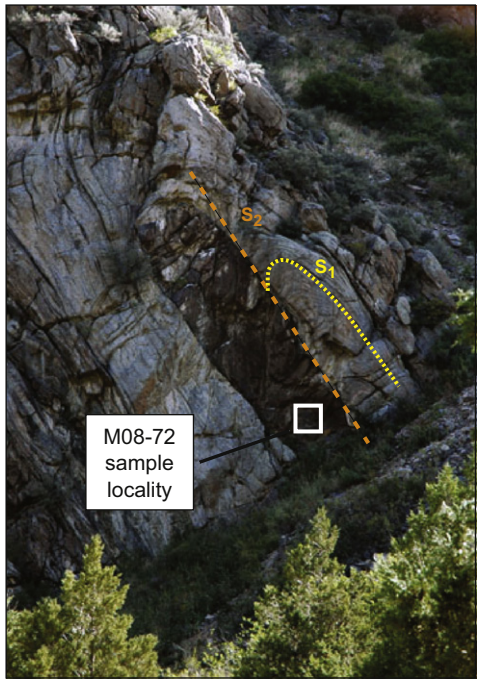

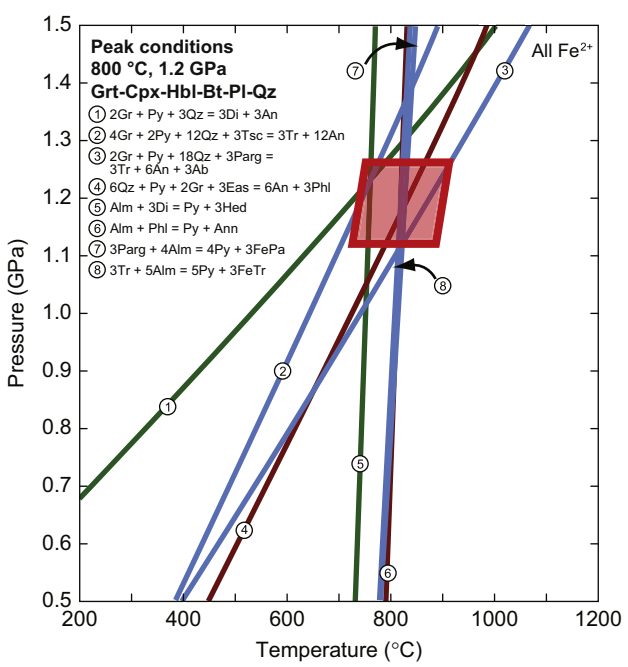

Fig. 2. (A) Simplified geologic map of southwestern Montana showing the location of major basement-cored Laramide uplifts, the Tobacco Root batholith, and sample M08-72. Also shown are the locations of biotite, muscovite, and hornblende $^{40}Ar/^{39}Ar$ (symbols with bold outlines) and K–Ar (symbols with thin outlines) dates from Hayden and Wehrenberg (1960), Giletti (1966), Marvin and Dobson (1979), Erslev and Sutter (1990), Jacob (1994), King (1994), Harlan et al. (1996), Kovaric et al., 1996, Brady et al., (1998, 2004), and Roberts et al. (2002). See table 1 of Brady et al. (2004) for a detailed compilation of Tobacco Root Mountains and vicinity Ar data. Giletti's Line, of Giletti (1966), is plotted as a dashed black line, separating K–Ar dates that were completely or partially reset in the Paleoproterozoic to the northwest from those that were not reset to the southeast. (B) Field photograph of the granulite-facies mafic dike from which sample M08-72 was taken with form lines for the early, folded fabric (S_1) and the later, steeply dipping fabric (S_2). (C) P–T diagram showing the results of quantitative thermobarometry for sample M08-72.

Montana (Fig. 2A; Hayden and Wehrenberg, 1959; Giletti, 1966; Marvin and Dobson, 1979), with newer $^{40}Ar/^{39}Ar$ data locally requiring temperatures of at least 500–550 °C (Jacob, 1994; Harlan et al., 1996; Kovaric et al., 1996; Brady et al., 1998; Roberts et al., 2002), the timing and extent to which high-grade metamorphism (temperatures >700 °C) impacted rocks across this region are still unclear. Additional regional thermal perturbations include the emplacement of volcanic and intrusive suites in Cretaceous and Tertiary time (Fig. 1).

Mafic dikes of the Northern Madison Range are well-exposed in Bear Trap canyon, along the Madison River (Fig. 2). Mafic dikes intrude Archean garnet and biotite-bearing quartzofeldspathic gneisses and garnet amphibolite. The $\sim$310 km^2 Tobacco Root batholith is exposed west of Bear Trap Canyon in the eastern and central Tobacco Root Mountains. It is composed of granitic to dioritic intrusive rocks and yields K–Ar biotite dates of 77 ± 2–72 ± 2 Ma (1σ errors) (Fig. 1 and Fig. 2A; Vitaliano et al., 1980).

3. Sample, methods and results

3.1. Sample M08-72

The analyzed sample (M08-72) was collected from the core of an $\sim$3 m-wide mafic dike in Bear Trap canyon (Fig. 2A and B). The sample contains early relict orthopyroxene and an equilibrium peak assemblage of Grt+Cpx+Hbl+Bt+Pl+Qz+Ilm, with accessory Ap and Zrn (abbreviations of Whitney and Evans, 2010). This dike was emplaced into a Pl+Bt+Qz $\pm$ Grt gneissic host. The dike cross-cuts an early, southwest-striking, shallowly dipping, folded fabric preserved in the host gneiss (S_1) but also contains a penetrative, northeast-striking, moderately dipping deformation fabric (S_2) that parallels the dike-host gneiss contact (Fig. 2B). The margins of the dike have been retrogressed to Hbl–Pl and the dike is boudinaged (Fig. 2B). Quantitative thermobarometry of the dike indicates peak metamorphic conditions of 1.2 ± 0.1 GPa and 800 ± 50 °C (Fig. 2C; mineral compositions, details of thermobarometry calculations, and associated X-ray compositions maps in Supplemental Material, S1).

3.2. Automated mineralogy, zircon imaging, and zircon selection

Identification and textural characterization of zircons were facilitated by in situ automated mineralogical analysis. We employed automated scanning electron microscope analysis (QEMSCAN) conducted at the Advanced Mineralogy Research Center at the Colorado School of Mines. QEMSCAN is a scanning electron microscope (SEM)-based analysis system that simultaneously collects energy dispersive X-ray spectrometer (EDS) spectra and calibrated backscatter electron (BSE) intensity information (Hoal et al., 2009). At each point in an automated map, the system collects a BSE signal and an EDS spectrum to make a phase identification based on prescribed BSE values and elemental intensities. A similar zircon search routine was used by Sack et al. (2011). Instrument operating conditions include 25 kV

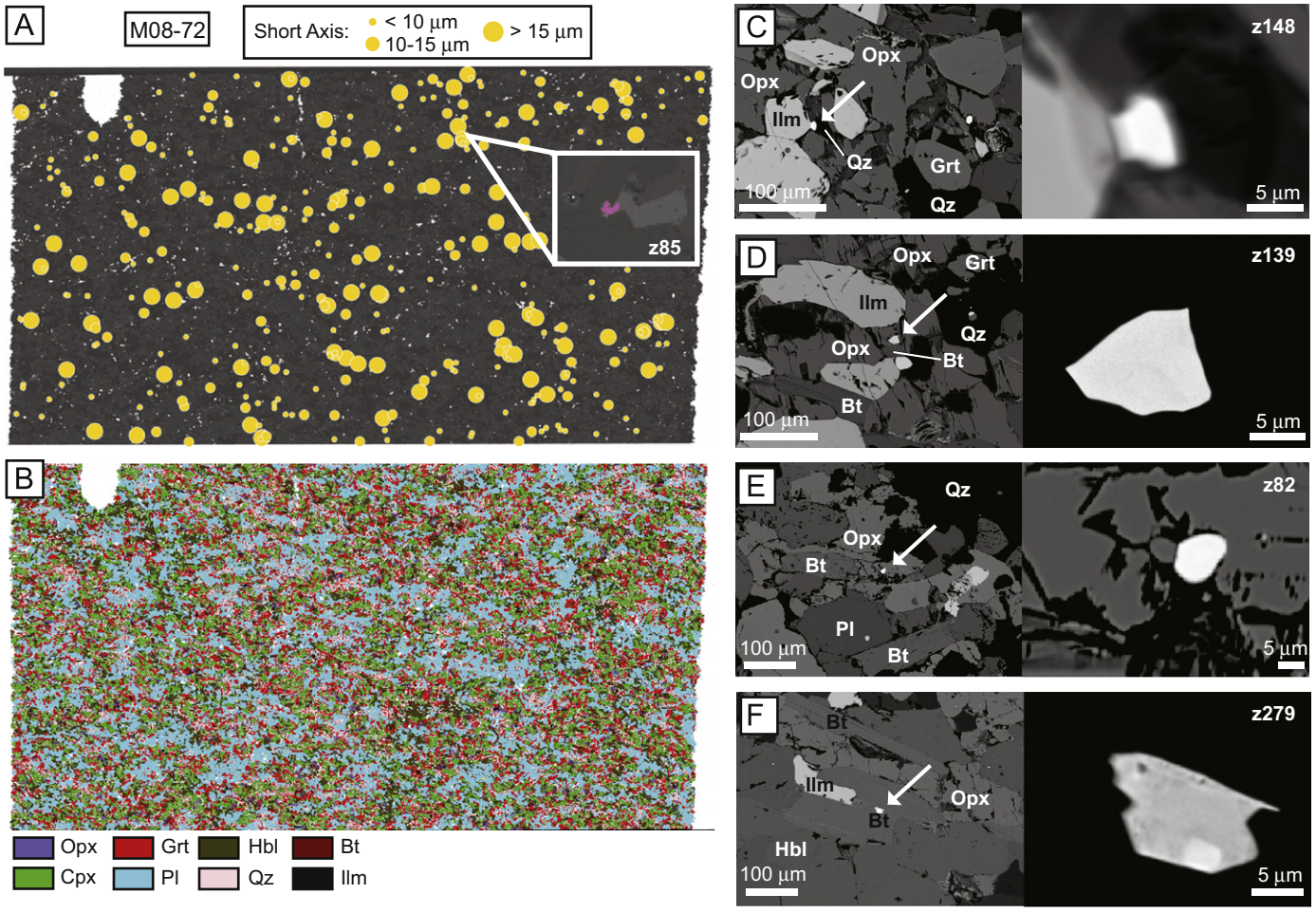

Fig. 3. M08-72 QEMSCAN thin section maps showing (A) location of zircons classified by short axis dimension against a composite BSE image, and (B) simplified modal mineralogy. Enlarged inset in (A) is an example of an analyzed zircon as it appears in QEMSCAN. (C–F) BSE images, at two scales, depicting the textural setting and morphology of a subset of the analyzed zircons. The smallest analyzed zircon is (C). White arrows highlight the location of the zircon grains.

Table 1
SIMS U–Pb zircon analyses from M08-72 (UTM 0453791E, 5046873N). Errors are given at 1-sigma.

Grain[a]	Textural Setting	Max. axis[a] (μm)	Min. axis[b] (μm)	$^{206}Pb/^{238}U$	% ±	$^{207}Pb/^{235}U$	% ±	rho [c]	$^{207}Pb/^{206}Pb$	% ±	U (ppm)	$^{206}Pb^{*}$ [d] (%)	Dates (Ma)						
													$^{206}Pb/^{238}U$	±	$^{207}Pb/^{235}U$	±	$^{207}Pb/^{206}Pb$	±	% Discordance
(A) Within unfractured quartz																			
z214	Qz	10	8	0.2863	0.90	4.1940	13.40	0.93	0.1062	0.13	1700	99.3	1623	45	1673	26	1736	22	7
z271	Qz	23	12	0.2862	0.75	4.2130	11.10	0.99	0.1068	0.05	1495	100.0	1622	37	1677	22	1745	8	7
z272	Qz	11	8	0.3171	1.04	4.7080	15.20	1.00	0.1077	0.03	1330	100.0	1775	51	1769	27	1761	5	0
(B) In phases with fractures and cleavage planes																			
z82	Opx	11	7	0.0778	0.29	0.9899	30.10	0.67	0.0923	2.59	1340	73.2	483	18	699	153	1473	531	67
z127	Qz	10	8	0.0654	0.26	1.2310	4.95	0.29	0.1365	0.65	1608	98.8	408	16	815	23	2184	83	81
z279	Bt	15	8	0.0504	0.12	0.6440	2.38	0.78	0.0927	0.22	2214	97.8	317	7	505	15	1481	45	79
(C) Along grain boundaries																			
z13	gb [e]	28	20	0.0696	0.20	0.9792	4.28	0.86	0.1020	0.24	1631	97.1	434	12	693	22	1661	44	74
z21	gb	10	8	0.1520	0.35	2.2600	5.19	0.89	0.1078	0.12	1062	99.1	912	20	1200	16	1763	20	48
z35	gb	7	5	0.0936	0.31	1.3100	4.55	0.91	0.1015	0.15	1751	99.9	577	18	850	20	1652	27	65
z76	gb	13	7	0.0749	0.25	1.0420	6.54	0.77	0.1009	0.43	1493	94.5	466	15	725	33	1641	79	72
z79	gb	25	12	0.2676	0.77	3.9150	11.90	0.98	0.1061	0.06	1049	99.3	1529	39	1617	25	1733	10	12
z85	gb	36	13	0.1147	0.31	1.6340	4.49	0.99	0.1033	0.05	1462	99.9	700	18	984	17	1685	8	58
z87	gb	10	8	0.1511	0.38	2.1630	6.33	0.93	0.1038	0.11	1205	97.3	907	21	1169	20	1693	20	46
z138	gb	24	22	0.1370	0.32	1.9820	4.93	0.99	0.1049	0.04	1110	99.4	828	18	1109	17	1712	8	52
z139	gb	13	10	0.1307	0.36	2.1360	24.40	0.74	0.1186	1.14	1140	91.3	792	21	1161	79	1935	172	59
z147	gb	38	18	0.0918	0.16	1.3100	7.97	0.62	0.1035	0.54	1594	97.2	566	9	850	35	1687	96	66
z148	gb	6	4	0.0786	0.13	1.0450	3.05	0.76	0.0965	0.19	1615	98.2	488	8	727	15	1557	37	69
z223	gb	30	10	0.0853	0.20	1.1780	7.18	0.49	0.1001	0.54	1516	95.8	528	12	790	34	1626	100	68
z269	gb	34	22	0.0772	0.17	1.0690	2.51	0.96	0.1004	0.06	1419	99.8	480	10	738	12	1631	12	71
z274	gb	12	10	0.1315	0.36	2.0450	18.30	0.69	0.1128	0.83	1515	94.2	796	20	1131	61	1845	133	57
z288	gb	12	9	0.0551	0.21	0.7097	8.64	0.71	0.0935	0.92	2817	91.4	346	13	545	51	1498	187	77
z289	gb	14	14	0.0542	0.09	0.7447	6.77	0.31	0.0996	0.87	1776	83.2	340	6	565	39	1617	162	79
z306	gb	36	25	0.0549	0.10	0.7486	1.36	0.98	0.0989	0.04	1706	99.8	345	6	567	8	1603	7	79
z311	gb	12	10	0.0445	0.07	0.5797	1.64	0.34	0.0945	0.26	1806	96.7	281	4	464	11	1519	51	82
z322	gb	20	15	0.1164	0.16	1.6680	2.16	0.92	0.1040	0.05	10279	99.4	710	9	997	8	1696	10	58

Decay constants: $\lambda(^{238}U) = 1.55125 \times 10^{-10}\ a^{-1}$; $\lambda(^{235}U) = 9.8485 \times 10^{-10}\ a^{-1}$; $\lambda(^{232}Th) = 4.9475 \times 10^{-11}\ a^{-1}$; $^{207}Pb/^{235}U$ ages are calculated from the measured radiogenic ^{207}Pb, corrected for common Pb, and measured ^{238}U divided by the $^{238}U/^{235}U$ abundance ratio of 137.88. U/Pb relative sensitivity was calibrated by UO_2/U. AS3 zircon standard analyzed during a May 12–13, 2010 session yielded a weighted mean $^{207}Pb/^{206}Pb$ date of 1073 ± 17 Ma (95% confidence; MSWD = 0.93) and a weighted mean $^{206}Pb/^{238}U$ date of 1095 ± 14 Ma (95% confidence; MSWD = 0.68). AS3 standard analyzed during a March 3, 2011 session yielded a weighted mean $^{207}Pb/^{206}Pb$ date of 1085 ± 19 Ma (95% confidence; MSWD = 0.96) and a weighted mean $^{206}Pb/^{238}U$ date of 1104 ± 28 Ma (95% confidence;MSWD = 0.18). Uncertainties in the reported analyses do not include error on the primary reference zircon or decay constant error.

[a] Max. axis = maximum axis dimension.
[b] Min. axis = minimum axis dimension.
[c] rho = correlation coefficient of error ellipses.
[d] Pb* = radiogenic Pb value, corrected for common Pb, in percent.
[e] gb = grain boundary.

accelerating voltage, 5 nA sample current, 0.25–0.5 μm beam size. An advantage of automated mineralogical analysis over X-ray elemental analysis is the far more rapid generation of whole thin section maps (<30 min with a 4 μm pixel dimension in our case). This facilitates quick identification of the primary phases and general texture via the BSE base map, and also rapidly confirms the presence, textural setting, and approximate grain size of accessory minerals as small as 4 μm.

QEMSCAN was used to create two maps of a single thin section from M08-72. The first map highlights the location of zircons (4 μm step-size; Fig. 3A) and the second is a complete map of modal mineralogy (20 μm step-size; Fig. 3B). A total of 376 zircons were identified in thin section and classified according to size (Fig. 3A). Approximately 50, 30, and 20% of the grains have short axes of <10 μm, 10–15 μm, and >15 μm, respectively. The maximum axis of the largest identified zircon is 38 μm. The two thin section maps were superimposed in concert with petrographic analysis to evaluate the textural setting of the zircons. Most zircons are located along grain boundaries and intersections of Grt, Cpx, Opx, Bt, Hbl, Pl, Qz, and Ilm. Several grains are contained entirely within Opx, Bt, or Qz. A subset of zircons was imaged with BSE using a JEOL JXA 8600 electron microprobe at the University of Colorado at Boulder. Most grains appear unzoned or exhibit minimal but irregular zoning patterns in BSE. We attempted to image the grains with cathodoluminescence (CL) on the JEOL 5800LV SEM at the University of Wyoming, but the grains did not luminesce.

A set of 25 zircon grains was selected for U–Pb SIMS analysis based on grain size, morphology, and textural setting. BSE images of the analyzed zircons are cataloged in Fig. 3C–F and Fig. S2. Of the target grains, 15 have a minimum axis dimension ≤ 10 μm (Table 1). The smallest dated grain is 6×4 μm^2 (z148, Fig. 3C). The largest dated grain is 36×25 μm^2, and is one of the largest grains of the entire zircon population (z306, Fig. S2S). Nineteen zircons are located along grain boundaries, including 7 spatially associated with Opx, 6 associated with Grt, 4 associated with Hbl, Pl, and Qz, and 2 associated with Bt. Of the zircons associated with or included in Bt, two zircons are rounded to subhedral and appear to have been overgrown by biotite (e.g., z306; Fig. S2S). Of the remaining 6 zircons, one grain (z82) is located within an Opx characterized by fractures parallel to cleavage planes (Fig. 3E). Another zircon is housed entirely within Bt and has a morphology suggesting zircon growth may have exploited the biotite 001 cleavage plane (z279; Fig. 3F). Finally, 4 of these 6 zircons zircons are located completely within quartz (z271, z272, z214, z127; Fig. 4 and Fig. S2). Two (z271, z272) are in the same quartz grain (Fig. 4B) and one (z127) occurs along an open fracture (Fig. 4C). Most zircon grains exhibit ovular or irregular morphology. Of the analyzed grains, 17 zircons lack internal zoning and 7 exhibit minor, irregular, or patchy zoning in BSE. One zircon is an exception (z322) and displays two distinct domains: an inner core riddled with inclusions and an outer, inclusion-free domain (Fig. S2U).

3.3. SIMS U–Pb analysis and results

The M08-72 thin section was trimmed to pieces <7 mm in size using a low speed diamond saw. These pieces were then mounted in epoxy in a Teflon ring with an inner diameter of 2.54 cm, polished, cleaned, and covered with a nm-scale coat of conductive Au following the procedures outlined in Schmitt et al. (2010). Each mount also contained up to 5 grains of zircon standard AS3. Target grains were photographed and documented in both plane and cross-polarized light, both with and without a Au-coat to assist in locating zircons during SIMS analytical work.

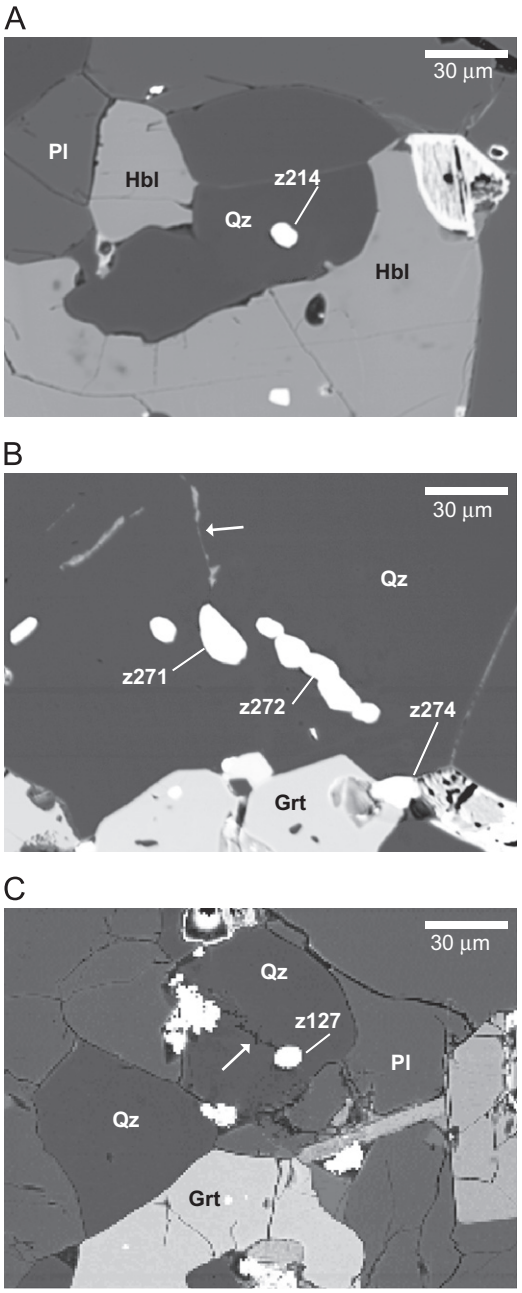

Fig. 4. BSE images of quartz-hosted zircons, (A) z214, (B) z271 and z272, and (C) z127. In (B), z274 is located at a grain boundary between quartz and garnet, and the white arrow highlights the location of an annealed fracture within quartz in contact with z271. White arrow in (C) points at an open fracture within quartz in contact with z127.

We used the high-sensitivity CAMECA ims 1270 ion microprobe at the University of California, Los Angeles in three analytical sessions during two visits to the lab facility separated by nine months. Recent advances in the SIMS technique improve upon the spatial resolution and ion yield of the conventional SIMS method (Schmitt et al., 2010), making this the optimal tool for obtaining in situ, high-resolution U–Pb geochronological data on small (≤ 10 μm) zircons. In this refined approach, zircons are identified using the CAMECA ims 1270 imaging capabilities and the Hf signal to ensure that the dominant signal of the U and Pb analysis is from the target zircon grain alone, even when the $\sim$20 μm primary beam diameter analysis pit encompasses both the zircon and a portion of the adjacent minerals (Fig. S3). The field aperture of the ims 1270 is adjusted to subsample secondary ions emitted

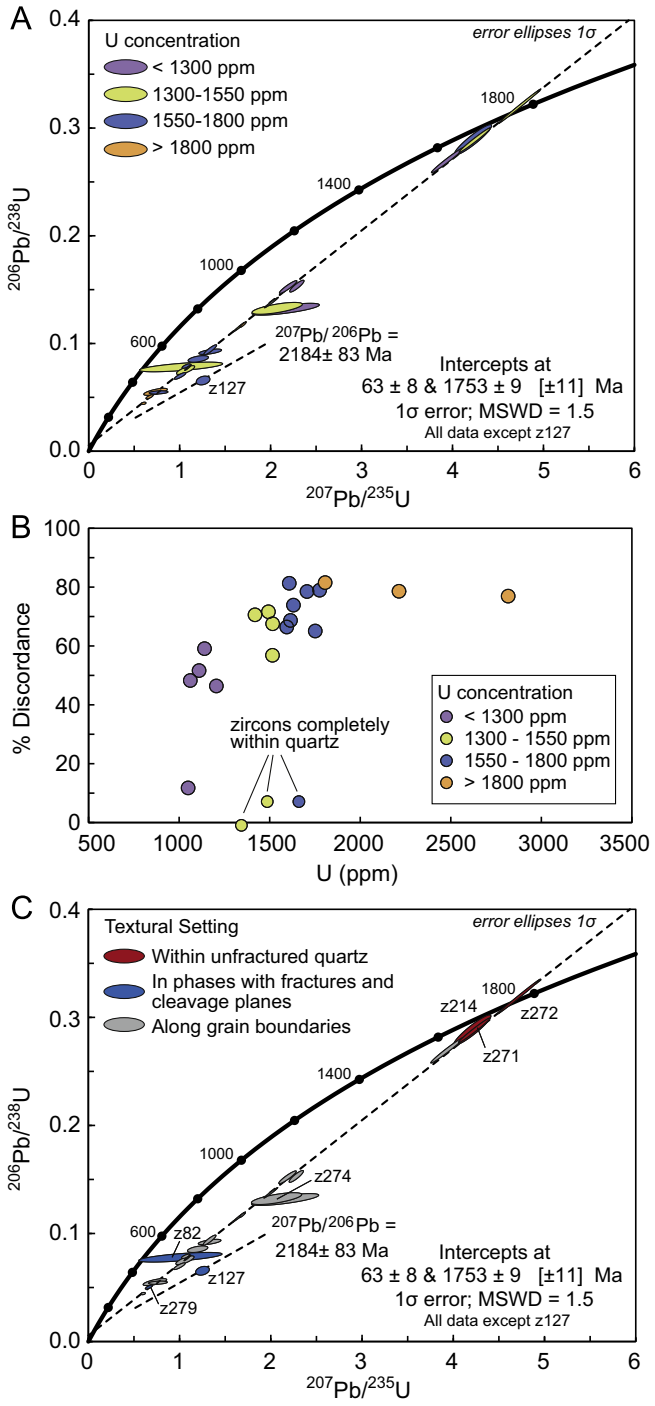

Fig. 5. (A) U–Pb concordia diagram for M08-72 with data distinguished by U concentration. (B) Percent discordance plotted as a function of U concentration for each group in (A). z322 is not plotted because the analysis is characterized by an anomalous U concentration due to U-rich inclusions. (C) U–Pb concordia diagram for M08-72 with data classified by zircon textural setting. The three most concordant analyses are contained completely within quartz, and are outliers from the percent discordance trend in (B). Analyses mentioned specifically in text are noted. Errors ellipses and intercepts are 1σ.

from the interior of the pit. This allows for analysis of zircon grains with a minimum dimension as small as 4 μm at radiogenic yields typically $>95\%$ for $^{206}Pb^*$ (radiogenic Pb). Narrowing the field aperture also assists in suppressing common Pb derived from the host minerals. In addition, the sample surface is flooded with oxygen gas, because enriching the sample surface layer in oxygen has been demonstrated to enhance the Pb* yield for sputtering of zircon by a factor of two. The instrument operating conditions and procedures performed to optimize secondary ion yields for the present study are described in detail by Grove et al. (2003) and Schmitt et al. (2010). Multiple analyses of zircon standard AS3 were performed at the beginning and end of each analytical session and between every 3 to 7 sample analyses.

We acquired one analysis for each of the 25 selected zircons because of the small size of the target grains. The results show a range of dates and U concentrations. Analytical results are reported in Table 1. All but one of the analyses define a discordia array with an upper intercept of 1753 ± 9 Ma and a lower intercept of 63 ± 8 Ma (Fig. 5A; 1σ error; MSWD = 1.5). One grain, z127, falls off this chord with a $^{207}Pb/^{206}Pb$ of 2184 ± 83 Ma (Fig. 5A, 1σ error). Percent discordance varies between 0 and 82% (Table 1). U concentration ranges from 1049 to 2817 ppm. Zircon z322 is an outlier with a U concentration of 10279 ppm, likely due to analysis of the grain's core that is filled with BSE-bright (Fig. S2U) and presumably U-rich inclusions.

4. Discussion

4.1. Influence of radiation damage and shielding on Pb loss from zircon

The discordance of the U–Pb data shows a relationship with both zircon U concentration and textural setting. Most data (22 of 25 analyses) display a positive correlation between discordance and U concentration for U values less than ~1600 ppm, with the trend flattening out at higher U (Fig. 5A and B). Within this suite, the two lowest U grains (1049–1062 ppm) are the most concordant (12–48%) and the three highest U grains (>1800 ppm) are the most discordant ($\geq 77\%$). Nineteen of these zircons are located along grain boundaries (e.g., Fig. 3C and D, Fig. S2). Three zircons occur in host minerals characterized by open fractures or cleavage planes (z127 in fractured quartz, z279 in biotite, and z82 in fractured orthopyroxene; Fig. 3 and Fig. S2). In contrast, the three zircons that do not conform to this U concentration pattern are either encapsulated completely within unfractured quartz (z214, z272), or in quartz with an annealed fracture (z271) (Fig. 4 and Fig. 5B and C). These three zircons yield the most concordant analyses ($\leq 7\%$) of the entire dataset, although they have U comparable to matrix zircons that are 67–79% discordant (Figs. 4 and 5). We find no correlation between zircon size and discordance even within groups of restricted U concentration, although this may reflect the randomness of thin section intersection with the zircon crystals that hinders reliable estimation of maximum zircon dimensions.

The upper intercept of the U–Pb discordia array indicates zircon growth at 1753 ± 9 Ma, likely during high-grade metamorphism as discussed in the next section. The lower intercept at 63 ± 8 Ma overlaps within 1σ uncertainty the K–Ar biotite dates of 77 ± 2–72 ± 2 Ma (1σ uncertainty; Vitaliano et al., 1980) for the large (~310 km^2 mapped exposure) Tobacco Root batholith located <10 km from the study area (Fig. 1 and Fig. 2A), pointing toward batholith emplacement as the cause of discordia array development. Although K/Ar and $^{40}Ar/^{39}Ar$ hornblende, muscovite, and biotite data from basement cored uplifts near the study area are predominantly 1.8–1.6 Ga (blue symbols in Fig. 2A and associated references), distinctly younger dates in a halo around the Tobacco Root batholith document the thermal pulse associated with batholith intrusion (red symbols in Fig. 2A; Giletti, 1966; Roberts et al., 2002; Brady et al., 2004). Nominal closure temperatures based on experimental data for Ar diffusion are 500–550 °C for hornblende (Harrison, 1981), 425–450 °C for muscovite (Harrison et al., 2009), and 300–350 °C for biotite (Grove and Harrison, 1996) depending on composition.

Two samples located ~7 km southwest of the M08-72 locality in southern Bear Trap canyon (Fig. 2A) yield $^{40}Ar/^{39}Ar$ dates of 1272 ± 8 Ma and 83 ± 4 Ma for hornblende, and 72 ± 8 Ma for biotite (Roberts et al., 2002), while a biotite K–Ar date of 1620 ± 32 Ma (Hayden and Wehrenberg, 1960) is reported from ~10 km north of our sample locality (Fig. 2A). These results document spatial heterogeneity in the duration and intensity of peak temperatures from <300 °C to ~500 °C depending on proximity to the batholith. The internal consistency of Grt–Bt thermometry with that of Grt–Cpx and Grt–Hbl from M08-72 suggests that Cretaceous reheating of this sample was likely nearer the lower end of the 300–500 °C range.

Although discordia array development was surely caused by batholith intrusion, observations are inconsistent with a second phase of zircon growth at this time. Only a minority of zircons exhibit irregular but minimal zoning in BSE (Fig. 3C–F, Fig. S2). Analysis pits on all zircons unzoned in BSE that occur in the matrix or fractured host phases yield discordant data. Conversely, two of three analyses (z271, z272) of the zircons hosted in unfractured quartz yield the most concordant results of the dataset despite the presence of faint zoning in BSE (Figs. S2N and S2O). These observations suggest that the discordia array is not due to sampling of multiple chemically distinct age domains. In addition, the sample is taken from the dike interior (Fig. 2B) and preserves a well-developed high-grade metamorphic texture. We do not observe petrographic evidence for significant retrograde metamorphic reactions associated with a post-1750 Ma thermal event that might have induced growth of a second zircon generation. For example, although garnet exhibits minor rim depletion in Mg suggestive of limited late Fe–Mg diffusional exchange with other ferromagnesian minerals, the subhedral garnet morphology and the lack of Mn enrichment at the edges are consistent with negligible retrograde garnet resorption (Fig. S1).

Instead, several aspects of the dataset point toward a radiation damage-enhanced Pb loss mechanism for generation of the discordia array. The U–Pb data from the zircons in fractured host grains and the matrix exhibit the classic relationship between higher U concentration and greater discordance that has been considered diagnostic of radiation damage-enhanced Pb loss (e.g., Silver and Deutsch, 1963; Krogh and Davis, 1975). The zircons do not luminesce in CL, as expected for significantly radiation damaged zircon grains in which CL is suppressed (Nasdala et al., 2002). Alpha dosage calculations also indicate that the zircons are strongly radiation damaged. Zircons accumulate radiation damage at temperatures below the critical amorphization temperature of ~360 °C (Meldrum et al., 1998). The regional background $^{40}Ar/^{39}Ar$ and K–Ar biotite dates (blue symbols in Fig. 2A and associated references) of 1.6–1.7 Ga indicate that the zircons were at temperatures less than ~300–350 °C and accumulating radiation damage for ~1.6 Ga until the thermal pulse associated with ca. 70 Ma Tobacco Roots batholith emplacement. Estimates of radiation damage alpha dosage computed using the equation of Holland and Gottfried (1955), assuming a 1.6 Ga time interval, and ignoring the contribution from Th range from 5.9149×10^{18} α/g to 1.5947×10^{19} α/g for the lowest and highest U zircons, respectively. These dosages exceed the typically observed threshold at which zircons become metamict (Geisler et al., 2003).

Although undamaged zircon has a nominal closure temperature of ~900 °C, experimental data demonstrates that radiation damage accumulation in zircon substantially lowers the Pb retentivity so that the closure temperature for metamict zircon may be no greater than a few hundred °C (e.g., Cherniak and Watson, 2000). The ~300–350 °C temperatures likely attained by our sample during the Cretaceous thermal pulse and the correlation between U and discordance in the dataset point toward this mechanism of enhanced volume diffusion in radiation damaged zircon. In this case, higher U zircons with greater radiation damage become less retentive to Pb and will undergo greater fractional Pb loss in response to a thermal pulse than lower U zircons with less damage accumulation. The recognition that the three zircons completely encapsulated in unfractured quartz yield the most concordant analyses of our dataset despite U concentrations comparable to matrix zircons suggests that textural armoring shielded these zircons from Pb loss. The contrast in discordance between quartz-hosted z271 and z272 (0, 7% discordance) with grains such as z274 (57% discordance) located along the boundary between this same quartz grain and the adjacent garnet supports this hypothesis (Fig. 4B). Although z271 is in contact with an annealed fracture in quartz that is visible in BSE, this fracture appears to have had little influence on Pb loss from this grain, suggesting that the fracture was not open at the time of the Pb loss event. In contrast, although z127 is also located completely within quartz, the zircon resides along an open fracture that is obvious both optically and in BSE. The z127 analysis is 81% discordant, consistent with facilitation of Pb loss by the presence of the open fracture (Fig. 4C). Together these observations suggest that the concordant and near-concordant results for the zircons in quartz are due to protection from Pb loss by the encapsulating grain, whereas the greater discordance of zircons located in fractured host grains and along grain boundaries is due to the presence of pathways for Pb migration during the Pb loss event. It is possible that the analytical spot sampled both the target zircon and some lesser portion of the host quartz grain, such that some fraction of the radiogenic Pb could have been analyzed from outside the zircon along the grain boundary or in the quartz. However, regardless of the exact location of the Pb, it is clear that it was mostly retained within the analysis site, suggesting that the zircons housed completely within unfractured quartz lacked fast pathways for the Pb to readily escape from the zircon and its immediate surroundings.

If the interpretation of enhanced volume diffusion in radiation damaged zircon is correct, this study would be the first to provide evidence for thermal shielding of zircons from Pb loss. Previous research on shielding effects in the U–Pb system has been largely empirical (Dahl, 1997), focused primarily on textural armoring of monazites from later recrystallization (e.g., DeWolf et al., 1993; Zhu et al., 1997; Montel et al., 2000), or emphasized shielding of zircon from interaction with crustal melts (e.g., Sergeev et al., 1995; Watson, 1996), all of which are distinct from the phenomenon of shielding of U–Th rich phases from Pb loss due to thermal effects alone. Few geo- or thermochronological datasets of any kind have been used to convincingly argue for shielding from thermal resetting. Perhaps the only example is an $^{40}Ar/^{39}Ar$ thermochronology study of a polymetamorphic gneiss that documented a discrepancy in dates between garnet-hosted and matrix biotite. This observation lead the authors to suggest that biotite grains in contact with fractures in the host garnet and along grain boundaries were more susceptible to Ar loss via volume diffusion following a high-grade metamorphic event than those biotite crystals in garnet that were thermally shielded from Ar loss (Kelley et al., 1997).

Other non-diffusional mechanisms, such as fluid-assisted processes (e.g., Geisler et al., 2007), can also induce Pb loss from zircons. An alternative interpretation of our results is that a fluid phase was responsible for the Pb loss, with greater Pb removed from the more damaged zircons, thus generating the correlation between U and discordance observed in our dataset. In this scenario, the limited Pb loss from the quartz-hosted zircons would be due to the inability of the fluid to penetrate the host grains, with any fractures in the host grains providing conduits for the fluid. However, we do not observe significant textural evidence for fluid, and the intensity of the thermal pulse appears sufficient to induce volume diffusion in these damaged zircons without requiring the assistance of a fluid to explain the data.

4.2. Implications for regional Paleoproterozoic thermotectonism

Peak P–T constraints, textural setting, zircon morphology, structural observations, and U–Pb geochronology from M08-72 collectively suggest metamorphic zircon growth in Paleoproterozoic time during high-pressure metamorphism. Quantitative thermobarometry of the peak mineral assemblage Grt+Cpx+Hbl+Bt+Pl+Qz+Ilm yields metamorphic conditions of ~800 °C and ~1.2 GPa (Fig. 2C). The zircons are texturally associated with all minerals of this peak metamorphic assemblage, including partial inclusion in several garnet porphyroblasts (e.g., Fig. S2B). Zircon characteristics are most consistent with a metamorphic origin (Corfu et al., 2003), as the zircons are round, ovular, or irregular in shape, and either lack internal zoning or exhibit minor, patchy zoning (Fig. 3C–F, Fig. S2). The peak assemblage defines the S_2 fabric observed in the M08-72 mafic dike and adjacent host gneiss (Fig. 2B), and our field observations indicate that this penetrative fabric occurs in the orthogneisses, paragneisses, and other similar mafic dikes exposed throughout the Bear Trap Canyon area. Based on these lines of evidence, we consider the upper intercept of 1753 ± 9 Ma to represent the timing of high-pressure metamorphism and regional D_2 deformation.

Paleoproterozoic high-grade metamorphism has been documented both in Archean rocks and mafic dikes in adjacent basement-cored mountain ranges to the west. Archean gneisses and metapelites in the Tobacco Root Mountains yield temperatures as high as 750 °C and pressures up to 1.0 GPa (Cheney et al., 2004a) at ca. 1.7 Ga (Brady et al., 2004; Cheney et al., 2004b; Harms et al., 2004). Mafic dikes exposed in the Tobacco Root Mountains record pressures of 0.8–1.0 GPa and temperatures of 625–700 °C (Cheney et al., 2004a); these peak conditions are slightly lower than those determined for M08-72. U–Pb data from a population of rounded zircons from a Tobacco Root dike in the northwestern part of that range record a weighted mean $^{207}Pb/^{206}Pb$ SHRIMP date of 1763 ± 8 Ma (Mueller et al., 2004). This date is interpreted to represent the timing of high-grade metamorphism in the Tobacco Root Mountains (Mueller et al., 2004), and is statistically indistinguishable from our metamorphic zircon date from M08-72 in Bear Trap Canyon.

Together these data point to a regional high-grade tectonometamorphic event at ca. 1.75 Ga along the northwestern margin of the Wyoming craton. Previous workers in the Tobacco Root Mountains labeled this event the Big Sky Orogeny, reflecting an arc-continent collision associated with activity on the Great Falls Tectonic Zone (e.g., Harms et al., 2004). Our data extend the spatial extent and elevated P–T conditions associated with this event into the Northern Madison Range and indicate that rocks in the vicinity of Bear Trap Canyon may be exhumed from a deeper structural level than those in the Tobacco Root Mountains.

5. Conclusions

The ability to analyze in situ zircon crystals as small as 5 μm with retention of the petrographic context makes it possible to obtain chronological information from zircons that are undatable by conventional methods, allows effective linkage of zircon growth history with the tectonometamorphic evolution of the rock, and can provide new insights into aspects of zircon U–Pb systematics. We applied automated mineralogy coupled with modifications to the conventional SIMS U–Pb dating technique to extract U–Pb data from zircons in a metamorphosed mafic dike in the Northern Madison Range, Montana. Automated mineralogy mapping revealed >375 sub-20 μm zircons in a variety of textural settings in our dike thin section. Adjusting the field aperture of the CAMECA ims 1270 to subsample the analysis pit (Chamberlain et al., 2010; Schmitt et al., 2010) allowed us to analyze zircon grains with minimum dimensions as small as 4 μm at radiogenic yields typically >95% for ^{206}Pb.

The discordia array shows a clear correlation with both zircon U concentration and textural setting. The positive correlation between U and discordance for matrix zircons and those in fractured host phases, as well as no evidence for new zircon growth, lead us to interpret the discordia array to reflect radiation damage-enhanced Pb loss. The temporal overlap between the lower intercept at 63 ± 8 Ma and emplacement of the nearby Tobacco Root batholith suggests that the thermal pulse associated with intrusion induced the Pb loss. Three zircons encapsulated completely within unfractured quartz are the only analyses that overlap concordia despite U concentrations comparable to highly discordant matrix grains. The simplest interpretation is that the zircons were shielded from Pb loss at ca. 63 Ma due to armoring in quartz. Thermochronologic data suggest that sustained basement temperatures near our sample of no greater than ~300–500 °C during Tobacco Root batholith emplacement induced the variable magnitudes of fractional Pb loss observed in our dataset.

We interpret the concordant analyses, defining the upper intercept of 1753 ± 9 Ma, to represent the timing of high-pressure metamorphism and associated deformation in the northwestern Wyoming craton during regional tectonism along the Great Falls Tectonic Zone. Documentation and interpretation of this early metamorphic history was enabled in part because the quartz-encapsulated zircons were shielded from the effects of subsequent intrusive activity. Our data thus highlight the value of in situ analyses for unraveling the complex evolution of polymetamorphic rocks.

Acknowledgments

We thank Axel Schmitt (University of California, Los Angeles) and Kevin Chamberlain (University of Wyoming) for their advice and assistance with SIMS analyses. Sarah Appleby (Colorado School of Mines) is thanked for providing the QEMSCAN analysis. We appreciate the assistance of Norbort Swoboda-Colberg (University of Wyoming) and John Drexler (University of Colorado at Boulder) on the SEM and electron microprobe, respectively. We thank two anonymous reviewers for comments that improved the clarity of the manuscript. This research was supported by an NSF Graduate Research Fellowship and a University of Colorado Department of Geological Sciences Longley-Wahlstrom-Werner award and travel grant to AKA.

Appendix A. Supporting information

Supplementary data associated with this article can be found in the online version at http://dx.doi.org/10.1016/j.epsl.2012.04.025.

References

Bowring, S.A., Schmitz, M.D., 2003. High-precision U–Pb zircon geochronology and the stratigraphic record. Rev. Mineral. Geochem. 53, 305–326.

Brady, J.B., Cheney, J.T., Rhodes, A.L., Vasquez, A., Green, C., Duvall, M., Kogut, A., Kaufman, L., Kovaric, D.N., 1998. Isotopic geochemistry of Proterozoic talc occurances in Archean marbles of the Ruby Mountains, southwest Montana, USA. Geol. Mater. Res. 2, 41.

Brady, J.B., Kovaric, D.N., Cheney, J.T., Jacob, L.J., King, J.T., 2004. $^{40}Ar/^{39}Ar$ ages of metamorphic rocks from the Tobacco Root Mountains region, Montana. In: Brady, J., Burger, K., Cheney, J., Harms, T. (Eds.), Precambrian Geology of the Tobacco Root Mountains, vol. 377. Geological Society of America, Montana, pp. 131–149 (Special paper).

Chamberlain, K., Frost, C.D., Frost, R., 2003. Early Archean and Mesoproterozoic evolution of the Wyoming Province: Archean origins to modern lithospheric architecture. Can. J. Earth Sci. 40, 1357–1374.

Chamberlain, K.R., Schmitt, A.K., Swapp, S.M., Harrison, T.M., Swoboda-Colberg, N., Bleeker, W., Peterson, T.D., Jefferson, C.W., Khudoley, A.K., 2010. In situ U–Pb

SIMS (IN-SIMS) micro-baddeleyite dating of mafic rocks: method with examples. Precambrian Res. 183, 379–387.
Cheney, J.T., Brady, J.B., Tierney, K.A., DeGraff, K.A., Mohlman, H.K., Hatch, C.E., Steiner, M.L., Carmichael, S.K., Fisher, R.G.M., Tuit, C.B., Steffen, K.J., Cady, P., Lowell, J., Archuleta, L.L., Hirst, J., Wegmann, K.W., Monteleone, B., 2004a. Proterozoic metamorphism of the Tobacco Root Mountains, Montana. In: Brady, J., Burger, K., Cheney, J., Harms, T. (Eds.), Precambrian Geology of the Tobacco Root Mountains, vol. 377. Geological Society of America, Montana, pp. 105–129 (Special paper).
Cheney, J.T., Webb, A.A.G., Coath, C.D., McKeegan, K.D., 2004b. In situ ion microprobe $^{207}Pb/^{206}Pb$ dating of monazite from Precambrian metamorphic suites, Tobacco Root Mountains, Montana. In: Brady, J., Burger, K., Cheney, J., Harms, T. (Eds.), Precambrian Geology of the Tobacco Root Mountains, vol. 337. Geological Society of America, Montana, pp. 151–179 (Special paper).
Cherniak, D.J., Watson, E.B., 2000. Pb diffusion in zircon. Chem. Geol. 172, 5–24.
Corfu, F., Hanchar, J.M., Hoskin, P.W.O., Kinny, P., 2003. Atlas of zircon textures. Rev. Mineral. Geochem. 53, 468–500.
Cox, D.M., Frost, C.D., Chamberlain, K.R., 2000. 2.01-Ga Kennedy dike swarm, southeastern Wyoming: record of a rifted margin along the southern Wyoming province. Rocky Mt. Geol. 35, 7–30.
Dahl, P.S., 1997. A crystal-chemical basis for Pb retention and fission track annealing systematics in U-bearing minerals, with implications for geochronology. Earth Planet. Sci. Lett. 150, 277–290.
DeWolf, C.P., Belshaw, N., O'Nions, R.K., 1993. A metamorphic history from micron-scale $^{207}Pb/^{206}Pb$ chronometry of Archean monazite. Earth Planet. Sci. Lett. 120, 207–220.
Erslev, E.E., Sutter, J.F., 1990. Evidence for Proterozoic mylonitization in the northwestern Wyoming province. Geol. Soc. Am. Bull. 102, 1681–1694.
Frost, C.D., Frost, R., Chamberlain, K., Hulsebosch, T., 1998. The late Archean history of the Wyoming Province as recorded by granitic magmatism in the Wind River Range, Wyoming. Precambrian Res. 89, 145–173.
Gehrels, G.E., Valencia, V., Ruiz, J., 2008. Enhanced precision, accuracy, efficiency, and spatial resolution of U–Pb ages by laser ablation-multicollector-inductively coupled plasma-mass spectrometry. Geochem. Geophys. Geosyst. 9, Q03017.
Geisler, T., Rashwan, A.A., Rahn, M.K.W., Poller, U., Zwingmann, H., Pidgeon, R.T., Schleicher, H., Tomaschek, F., 2003. Low-temperature hydrothermal alteration of natural metamict zircons from the Eastern Desert, Egypt. Mineral. Mag. 67, 485–508.
Geisler, T., Schaltegger, U., Tomaschek, F., 2007. Re-equilibration of zircon in aqueous fluids and melts. Elements 3, 43–50.
Giletti, B.J., 1966. Isotopic ages from southwestern Montana. J. Geophys. Res. 71, 4029–4036.
Grove, M., Harrison, T.M., 1996. $^{40}Ar^{*}$ diffusion in Fe-rich biotite. Am. Mineral. 81, 940–951.
Grove, M., Jacobsen, C.E., Barth, A.P., Vucic, A., 2003. Temporal and spatial trends of late Cretaceous–early Tertiary underplating Pelona and related schist beneath southern California and southwestern Arizona. Geol. Soc. Am. Spec. Pap. 374, 381–406.
Harlan, S.S., Geissman, J.W., Premo, W.R., 2003. Paleomagnetism and geochronology of and Early Proterozoic quartz diorite in the southern Wind River Range, Wyoming, USA. Tectonophysics 362, 105–122.
Harlan, S.S., Geissman, J.W., Snee, L.W., Reynolds, R.L., 1996. Late Cretaceous remagnetization of Proterozoic mafic dikes, southern Highland Mountains, southwestern Montana: a paleomagnetic and $^{40}Ar/^{39}Ar$ study. Geol. Soc. Am. Bull. 108, 653–668.
Harlan, S.S., Premo, W.R., Unruh, D., Geissman, J.W., 2005. Isotopic dating of Meso- and Neoproterozoic mafic magmatism in southern Tobacco Root Mountains, Southwestern Montana. Precambrian Res. 136, 269–281.
Harms, T.A., Brady, J.B., Burger, H.R., Cheney, J.T., 2004. Advances in the geology of the Tobacco Root Mountains, Montana, and their implications for the history of the northern Wyoming province. In: Brady, J., Burger, K., Cheney, J., Harms, T. (Eds.), Precambrian Geology of the Tobacco Root Mountains, vol. 377. Geological Society of America, Montana, pp. 227–243 (Special paper).
Harrison, T.M., 1981. Diffusion of ^{40}Ar in hornblende. Contrib. Mineral. Petrol. 78, 324–331.
Harrison, T.M., Célérier, J., Aikman, A.B., Hermann, J., Heizler, M.T., 2009. Diffusion of ^{40}Ar in muscovite. Geochim. Cosmochim. Acta. 73, 1039–1051.
Hayden, R.J., Wehrenberg, J.P., 1959. Potassium–argon dating in western Montana. Geol. Soc. Am. Bull. 70, 1778–1779.
Hayden, R.J., Wehrenberg, J.P., 1960. A^{40}–K^{40} dating of igneous and metamorphic rocks in western Montana. J. Geol. 68, 94–97.
Henstock, T., Levander, A., Snelson, C., Keller, R., Miller, K.G., Harder, S., 1998. Probing the Archean and Proterozoic lithosphere of western North America. GSA Today 8 (1–5), 16–17.
Hoal, K.O., Appleby, S.K., Stammer, J.G., Palmer, C., 2009. SEM-based quantitative mineralogical analysis of peridotite, kimberlite, and concentrate. Lithos 112, 41–46.
Holland, H.D., Gottfried, D., 1955. The effect of nuclear radiation on the structure of zircon. Acta Crystallogr. 8, 291–300.
Ireland, T.R., Williams, I.S., 2003. Considerations in zircon geochronology by SIMS. Rev. Mineral. Geochem. 53, 215–241.
Jacob, L.J., 1994. A geochemical and geochronological characterization of the Indian Creek Metamorphic Suite in the Noble Lake area, south-central Tobacco Root Mountains, southwestern Montana. B.A. Thesis. Northampton, Massachusetts, Smith College, pp. 73.
Kelley, S.P., Bartlett, J.M., Harris, H.B.W., 1997. Pre-metamorphic Ar–Ar ages from biotite inclusions in garnet. Geochim. Cosmochim. Acta 61, 3873–3878.
King, J.T., 1994. A structural analysis of Archean gneisses in the Tobacco Root Mountains, southwestern Montana. B.A. Thesis. Amherst, Massachusetts, Amherst College, pp. 44.
Kovaric, D.N., Brady, J.B., Cheney, J.T., Grove, M., Jacob, L.J., King, J.T., 1996. $^{40}Ar/^{39}Ar$ evidence for reheating events affecting basement rocks in the Tobacco Root, Ruby, and Highland Mountains, SW Montana. Geol. Soc. Am. Abstr. Programs 29, 408.
Krogh, T.E., Davis, G.L., 1975. Alteration in Zircons and Differential Dissolution of Altered and Metamict Zircon, vol. 74. Carnegie Institution of Washington Publication (pp. 619–623).
Marvin, R.F., Dobson, S.W., 1979. Radiometric ages; compilation B, U.S. Geological Survey. Isochron/West 26, 3–30.
Meldrum, A., Boatner, L.A., Weber, W.J., Ewing, R.C., 1998. Radiation damage in zircon and monazite. Geochim. Cosmochim. Acta 62, 2509–2520.
Mogk, D.W., Mueller, P.A., Wooden, J.L., 1992. The significance of Archean terrane boundaries: evidence from the northern Wyoming Province. Precambrian Res. 55, 155–168.
Montel, J.-M., Kornprobst, J., Vielzeuf, D., 2000. Preservation of old U–Th–Pb ages in shielded monazite: example from the Beni Bousera Hercynian kinzigites (Morocco). J. Metamorph. Geol. 18, 335–342.
Mueller, P.A., Burger, H.R., Wooden, J.L., Heatherington, A.L., Mogk, D.W., D'Arcy, K., 2004. Age and evolution of the Precambrian crust of the Tobacco Root Mountains. In: Brady, J., Burger, K., Cheney, J., Harms, T. (Eds.), Precambrian Geology of the Tobacco Root Mountains, vol. 377. Geological Society of America, Montana, pp. 181–202 (Special paper).
Mueller, P.A., Shuster, R., Wooden, J.L., Erslev, E., Bowes, D., 1993. Age and composition of Archean crystalline rocks from the southern Madison Range: implications for crustal evolution in the Wyoming craton. Geol. Soc. Am. Bull. 105, 437–446.
Nasdala, L., Lengauer, C.L., Hanchar, J.M., Kronz, A., Wirth, R., Blanc, P., Kennedy, A.K., Seydoux-Guillaume, A.-M., 2002. Annealing of radiation damage and the recovery of cathodoluminescence. Chem. Geol. 181, 121–140.
Premo, W.R., Helz, R.T., Zientek, M.L., Langston, R.B., 1990. U–Pb and Sm–Nd ages for the Stillwater Complex and its associated sills and dikes, Beartooth Mountains, Montana: identification of a parent magma? Geology 18, 1065–1068.
Premo, W.R., Van Schmus, W.R., 1989. Zircon geochronology of Precambrian rocks in southeastern Wyoming and northern Colorado. In: Grambling, J.A., Tewksbury, B.J. (Eds.), Proterozoic Geology of the Southern Rocky Mountains, vol. 235. Geological Society of America, pp. 1–12 (Special paper).
Ramezani, J., Hoke, G.D., Fastovsky, D.E., Bowring, S.A., Therrien, F., Dworkin, S.I., Atchley, S.C., Nordt, L.C., 2011. High-precision U–Pb zircon geochronology of the Late Triassic Chinle Formation, Petrified Forest National Park (Arizona, USA): temporal constraints on the early evolution of dinosaurs. Geol. Soc. Am. Bull. 123, 2142–2159.
Roberts, H., Dahl, P., Kelley, S.A., Frei, R., 2002. New $^{207}Pb/^{206}Pb$ and $^{40}Ar/^{39}Ar$ ages from SW Montana, USA: constraints on the Proterozoic and Archean tectonic and depositional history of the Wyoming Province. Precambrian Res. 117, 119–143.
Sack, P.J., Berry, R.F., Meffre, S., Falloon, T.J., Gemmell, J.B., 2011. In situ location and U–Pb dating of small zircon grains in igneous rocks using laser ablation-inductively coupled plasma-quadrupole mass spectrometry. Geochem. Geophys. Geosyst. 12, Q0AA14.
Schmitt, A.K., Chamberlain, K.R., Swapp, S.M., Harrison, T.M., 2010. In situ U–Pb dating of micro-baddeleyite by secondary ion mass spectrometry. Chem. Geol. 269, 386–395.
Sergeev, S.A., Meier, M., Steiger, R.H., 1995. Improving the resolution of single-grain U/Pb dating by use of zircon extracted from feldspar: application to the Variscan magmatic cycle in the central Alps. Earth Planet. Sci. Lett. 134, 37–51.
Silver, L.T., Deutsch, S., 1963. Uranium-lead isotopic variations in zircons—a case study. J. Geol. 71, 721–758.
Snyder, G.L., Hughes, D.J., Hall, R.P., Ludwig, K.R., 1988. Distribution of Precambrian Mafic Intrusives Penetrating Some Archean Rocks of Western North America. U.S. Geological Survey Open File Report, vol. 36, pp. 89–125.
Stern, R.A., Berman, R.G., 2000. Monazite U–Pb and Th–Pb geochronology by ion microprobe, with an application to in situ dating of an Archean metasedimentary rock. Chem. Geol. 172, 113–130.
Tomkins, H.S., Williams, I.S., Ellis, D.J., 2005. In situ U–Pb dating of zircon formed from retrograde garnet breakdown during decompression in Rogaland, SW Norway. J. Metamorph. Geol. 23, 201–215.
Vitaliano, C.J., Kish, S.A., Towell, D.G., 1980. K–Ar dates and Sr isotopic values for rocks of the Tobacco Root batholith. Isochron/West 28, 13–15.
Watson, E.B., 1996. Dissolution, growth, and survival of zircons during crustal fusion: kinetic principles, geological models, and implications for isotopic inheritance. Trans. R. Soc. Edinb. Earth Sci. 87, 43–56.
Whitney, D.L., Evans, B.W., 2010. Abbreviations for names of rock-forming minerals. Am. Mineral. 95, 185–187.
Wooden, J.L., Mueller, P.A., 1988. Pb, Sr, and Nd isotopic compositions of a suite of Late Archean igneous rocks, eastern Beartooth Mountains: implications for crust-mantle evolution. Earth Planet. Sci. Lett. 87, 59–72.
Zhu, X.K., O'Nions, R.K., Belshaw, N., Gibb, A.J., 1997. Lewisian crustal history from in situ SIMS mineral chronometry and related metamorphic textures. Chem. Geol. 136, 205–218.